Pseudo-halide Anion Engineering for α-$FAPbI_3$ perovskite solar cells

Jaeki Jeong[1,2,4#], Minjin Kim[3#], Jongdeuk Seo[1#], Haizhou Lu[2,4#], Paramvir Ahlawat[5], Aditya Mishra[6], Yingguo Yang[7], Michael A. Hope[6], Felix T. Eickemeyer[2], Maengsuk Kim[1], Yung Jin Yoon[1], In Woo Choi[3], Barbara Primera Darwich[8], Seung Ju Choi[3], Yimhyun Jo[3], Jun Hee Lee[1], Bright Walker[9], Shaik M. Zakeeruddin[2], Lyndon Emsley[6], Ursula Rothlisberger[5], Anders Hagfeldt[4,10]*, Dong Suk Kim[3]*, Michael Grätzel[2]*, Jin Young Kim[1]*

[1]Department of Energy Engineering, Ulsan National Institute of Science and Technology (UNIST), UNIST-Gil 50, Ulsan, 44919, Republic of Korea.
[2]Laboratory of Photonics and Interfaces, Institute of Chemical Sciences and Engineering, École Polytechnique Fédérale de Lausanne (EPFL), CH-1015 Lausanne, Switzerland.
[3]Korea Institute of Energy Research (KIER), Nam-gu, Ulsan, 44776, Republic of Korea.
[4]Laboratory of Photomolecular Science, Institute of Chemical Sciences Engineering, École Polytechnique Fédérale de Lausanne (EPFL), CH-1015 Lausanne, Switzerland.
[5]Laboratory of Computational Chemistry and Biochemistry, Institute of Chemical Sciences and Engineering, École Polytechnique Fédérale de Lausanne (EPFL), CH-1015 Lausanne, Switzerland.
[6]Laboratory of Magnetic Resonance, Institute of Chemical Sciences and Engineering, École Polytechnique Fédérale de Lausanne (EPFL), CH-1015 Lausanne, Switzerland.
[7]Shanghai Synchrotron Radiation Facility (SSRF), Zhangjiang Lab, Shanghai Advanced Research Institute, Chinese Academy of Sciences, 239 Zhangheng Road, Shanghai 201204, P. R. China.
[8]Laboratory for Molecular Engineering of Optoelectronic Nanomaterials, École Polytechnique Fédérale de Lausanne (EPFL), CH-1015 Lausanne, Switzerland.
[9]Department of Chemistry and Research Institute of Basic Sciences, Kyung Hee University, Dongdaemun-gu, Seoul, 02447, Republic of Korea.
[10]Current address: Department of Chemistry, Ångström Laboratory, Uppsala University, Box 523, 751 20 Uppsala, Sweden.

[#]These authors contributed equally to this work.
*Correspondence to: anders.hagfeldt@epfl.ch, kimds@kier.re.kr, michael.graetzel@epfl.ch, jykim@unist.ac.kr.

Abstract

Metal halide perovskites of the general formular ABX_3 where A is a monovalent cation such as caesium, methylammonium or formamidinium, B stands for divalent lead, tin or germanium and X is a halide anion, have shown great potential as light harvesters for thin film photovoltaics. *(1-5)* Amongst a large number of compositions investigated, the cubic a-phase of formamidinium lead triiodide ($FAPbI_3$) has emerged as the most promising semiconductor for highly-efficient and stable perovskite solar cells (PSCs) *(6-9)*. Maximizing the performance of α-$FAPbI_3$ has therefore become of vital importance for the perovskite research community. Here, we introduce a new anion engineering concept that employs the pseudo-halide formate ($HCOO^-$) to supress anion vacancy electric defects present at grain-boundaries and the surface of the perovskite films and to augment their crystallinity, enabling PSCs to attain a record power conversion efficiency of 25.6 % (certified 25.2%), long-term operational stability and

intense electroluminescence with external quantum efficiencies over 10%. Our findings open up a direct route to eliminate the most abundant and deleterious lattice defects present in metal halide perovskites providing a facile access to solution processable films with unprecedented opto-electronic performance.

Main text

Perovskite solar cells (PSCs) have attracted much attention since their first demonstration in 2009 (*1-5*). There has been a rapid expansion of research on PSCs, driven by the low-cost solution processing and attractive optoelectronic properties, such as tuneable bandgap (*6*), high absorption coefficient (*10*), low recombination rate (*11*) and high mobility of charge carriers (*12*). Within a decade, the power conversion efficiency (PCE) of single junction PSCs progressed from 3% to a certified value of 25.5% (*13*), the highest for thin-film photovoltaics. Moreover, the long-term operational stability of PSCs exceeds now 1000 hours in full sunlight using additive and interface engineering strategies (*14,15*). Thus, PSCs show great promise for deployment as the next generation of photovoltaics.

Compositional engineering plays a key role in achieving highly-efficient and stable PSCs. In particular, mixtures of methylammonium lead triiodide ($MAPbI_3$) with formamidinium lead triiodide ($FAPbI_3$) have been extensively studied (*5,7*). Compared to $MAPbI_3$, $FAPbI_3$ is thermally more stable and has a bandgap closer to the Shockley-Queisser limit (*6*), rendering $FAPbI_3$ the most attractive perovskite layer for single junction PSCs. Unfortunately, thin $FAPbI_3$ films undergo a phase-transition from the black α-phase to a photoinactive yellow δ-phase below a temperature of 150 °C. Previous approaches to overcome this problem include mixing $FAPbI_3$ with a combination of MA^+, Cs^+ and Br^- ions, at the cost of blue-shifted absorbance and phase segregation under operational conditions (*7-9,16*).

Nevertheless, α-$FAPbI_3$ has recently emerged as the candidate of choice for highly-efficient and stable PSCs (*9,17,18*). We prepared α-$FAPbI_3$ by spin coating a precursor solution of $FAPbI_3$ mixed with excess MACl and achieved a certified efficiency of 23.48% for the mesoporous-structure $FAPbI_3$ PSC (*17*). Later, Min *et al*. reported that $FAPbI_3$ PSCs could be further stabilized with methylenediammonium dichloride ($MDACl_2$), resulting in a certified efficiency of 23.73% (*18*). By fully exploiting the absorption spectrum of $FAPbI_3$ together with proper light management, the short-circuit current density (J_{sc}) reached 26.7 mA/cm^2, approaching the theoretical maximum (*18*). However, the open-circuit voltage (V_{oc}) of ~1.15 V for $FAPbI_3$ PSCs still lags behind the radiative limit (*9,18*), implying that more work is needed to further reduce the defect density in the $FAPbI_3$ perovskite films to supress non-radiative recombination of charge carriers.

Br^-, Cl^-, and thiocyanate (SCN^-) anions, have been commonly used to improve the crystallinity and stability of perovskite films (*8,9,11,17-22*). Another pseudo-halide anion, formate ($HCOO^-$), has been investigated in connection with $MAPbI_3$ based PSCs (*23-26*). T. Moore *et al*. (*23*) and Seo *et al*. (*24*) reported that methylammonium formate, an ionic liquid, improves the quality of $MAPbI_3$ films by controlling the perovskite crystal growth, while K. Nayak *et al*. (*25*) reported that formic acid accelerates the crystallisation of MA cation-based perovskites by dissolving the perovskite colloids in the precursor solution. Similar findings were published by Meng *et al.* (26). Thus, the previous work mainly dealt with the effect of formate on the morphology, nucleation and growth of $MAPbI_3$. Recently, Khan *et al*. (27) reported highly fluorescent methylammonium lead bromide/formate mixture in water, but a fundamental understanding is missing.

Here, we uncover the key role of $HCOO^-$ anions in removing the halide vacancies, which are the predominant lattice defects in $FAPbI_3$ perovskite films. This enables the PCE of the PSC to pass over 25% combined with a high operational stability and external quantum efficiency (EQE) of electroluminescence exceeding 10%. Iodide vacancies are also the principle cause for the unwanted ionic conductivity of metal halide perovskites which exerts a deleterious effect on their operational stability. We provide new insight into the mode of formate intervention. Based on its size effect, formate is small enough to fit in the iodide vacancy (*22*), eliminating a prevalent and notorious defect in the metal halide perovskite that accelerates the nonradiative recombination of photogenerated charge carriers decreasing both the fill factor (FF) and V_{oc} of a solar cell. In addition, $FAPbI_3$ perovskite films with improved crystallinity and larger grain size were achieved by introducing 2% FAHCOO into the precursor solution. The defect passivation and the improved crystallinity are essential to attain the record efficiency and excellent stability demonstrated by our $FAPbI_3$-based PSCs.

The reference $FAPbI_3$ film, hereafter noted as "reference", was prepared as previously reported using a precursor solution containing a mixture of $FAPbI_3$ powder with 35 mol% additional MACl (*17*). For the formate doped $FAPbI_3$ (Fo-$FAPbI_3$) film, x mol% ($x \leq 4$) FAHCOO was added to the reference precursor solution. Experimental details are included in the supplementary materials (SM). In the later discussion, we quantify the amount of MA in the resulting perovskite composition to be 5%, but for simplicity, we will still refer to the sample as $FAPbI_3$ in the following text. Figure 1A shows the ultraviolet-visible (UV-Vis) absorption and photoluminescence (PL) spectra of the $FAPbI_3$ perovskite films. Identical absorption threshold and PL peak position were observed for all films, but there was an obvious decrease of the absorbance when 4% FAHCOO was added. Figure 1B shows the time-resolved photoluminescence (TRPL) of the $FAPbI_3$ perovskite films. The 2% Fo-$FAPbI_3$ perovskite film showed a slower PL decay than the reference which indicates a reduced non-radiative recombination rate due to a reduction of trap-mediated bulk or surface recombination. In contrast, the 4% Fo-$FAPbI_3$ perovskite film showed a faster PL decay than the reference. A full PL decay up to 4 μs is shown in fig. S1. A quantitative analysis of the TRPL is presented in Note 1 in the SM.

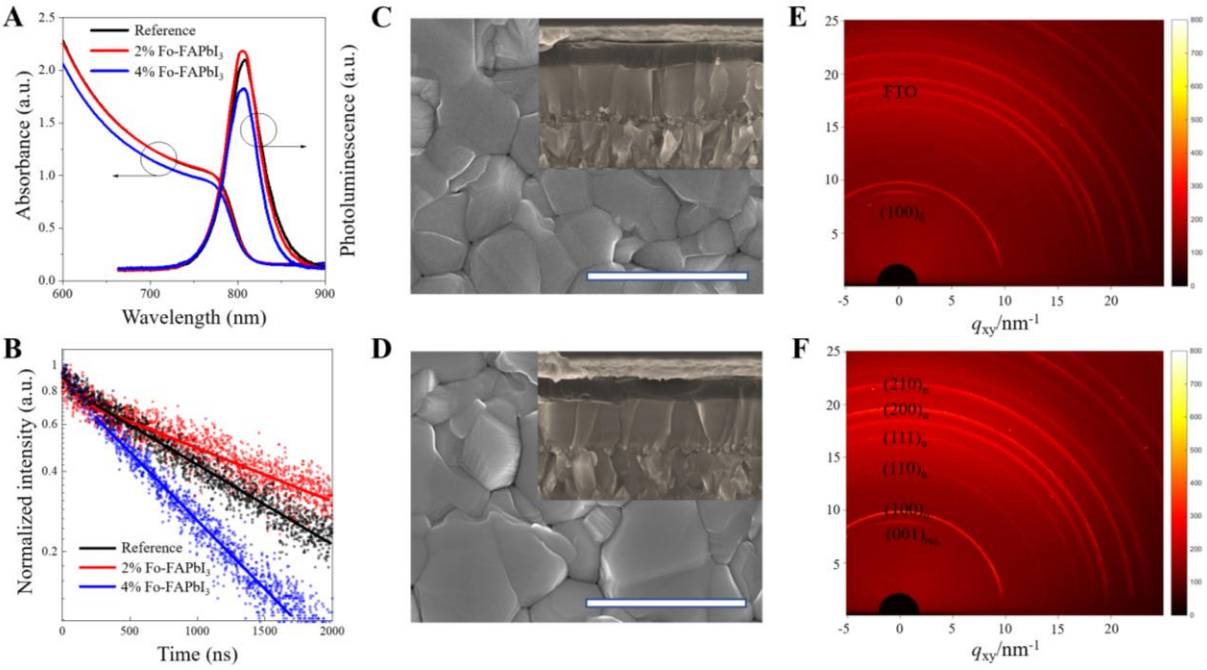

Figure 1. Characterisation of the $FAPbI_3$ films. (**A**) UV-Vis absorption and PL spectra of the $FAPbI_3$ films. (**B**) TRPL of the $FAPbI_3$ films. SEM images of the reference $FAPbI_3$ (**C**) and 2% Fo-$FAPbI_3$ (**D**) films (Scale bar is 2 μm, cross-sectional SEM images are inserted). 2D-GIXRD patterns of the reference (**E**) and 2% Fo-$FAPbI_3$ (**F**) films.

Scanning electron microscopy (SEM) measurements were performed to investigate the perovskite film morphology. Compared to the reference film (Fig. 1C), the 2% Fo-$FAPbI_3$ film (Fig. 1D) had a larger grain size of up to 2 μm. The inset pictures in Fig. 1, C and D, are the cross-sectional SEM images of the corresponding perovskite films. Both the reference and 2% Fo-$FAPbI_3$ films showed monolithic grains from the top to the bottom. Figure S2 shows the irregular and small grain size for the 4% Fo-$FAPbI_3$ films. Atomic force microscopy (AFM) measurements (fig. S3) showed a surface roughness of 41.66 and 57.47 nm for the reference and 2% Fo-$FAPbI_3$ films, respectively. The slightly increased surface roughness of the 2% Fo-$FAPbI_3$ film is mostly like due to the increased grain size.

X-ray diffraction (XRD) measurements (fig. S4) showed that the reference and Fo-$FAPbI_3$ perovskite films had identical peak positions at around 13.95 ° and 27.85 °, corresponding to the α-phase of $FAPbI_3$. However, the XRD pattern of the 4% Fo-$FAPbI_3$ film showed additional peaks which are assigned to fluorine doped tin oxide (FTO) substrates and different orientations of α-$FAPbI_3$. The broader and lower intensity diffraction peaks (resulting in higher relative noise level) indicate a poor crystallinity, which is consistent with the poor optical measurements of the 4% Fo-$FAPbI_3$ film above. Synchrotron-based two-dimensional grazing-incidence XRD (2D-GIXRD) measurements were also performed for the $FAPbI_3$ films at a relative humidity (RH) of ~100% at 30 ℃ in ambient air. Figure 1E clearly shows the presence of the δ-phase for the reference, while the δ-phase was absent in the 2% Fo-$FAPbI_3$ film (Fig. 1F). This provides strong evidence that the FAHCOO stabilizes the α-phase of $FAPbI_3$ against humidity. In addition, the full width at half maximum of the α-phase peak was decreased for the 2% Fo-$FAPbI_3$, hereafter noted as "target". The integrated 1D diffraction intensity is shown in fig. S5. We infer from these data that including FAHCOO in the synthesis of the $FAPbI_3$ films strongly enhances their crystallinity.

We performed solid state nuclear magnetic resonance (NMR) spectroscopy measurements in order to unravel the molecular mechanism of the improvements afforded by the $HCOO^-$ anions. We prepared the samples by mixing FAI and PbI_2 powders with 5 mol% extra FAHCOO using a mechano-synthesis method. MACl was not added to avoid broadening of resonances, affording greater resolution and therefore sensitivity to the local environments (details are given in the SM). The ^{207}Pb spectrum is sensitive to the nature of the anions coordinated to Pb^{2+} in the perovskite (*28*); Figure 2A shows the ^{207}Pb spectrum of α-$FAPbI_3$ which resonances at 1543 ppm. The addition of 5% FABr results in a notable shoulder on the low-frequency side of the ^{207}Pb resonance, as shown in Fig. 2A (b). Since $FAPbBr_3$ resonates at 510 ppm (*28*), the new ^{207}Pb environment has a slightly lower frequency than α-$FAPbI_3$. However, the ^{207}Pb resonance of the α-$FAPbI_3$ remained the same after adding 5% FAHCOO in the synthesis, which is strong evidence that $HCOO^-$ does not substitute for iodide anions on the α-$FAPbI_3$ lattice. This is also supported by the density functional theory (DFT) calculations of the formation energy shown in Note 2 in the SM.

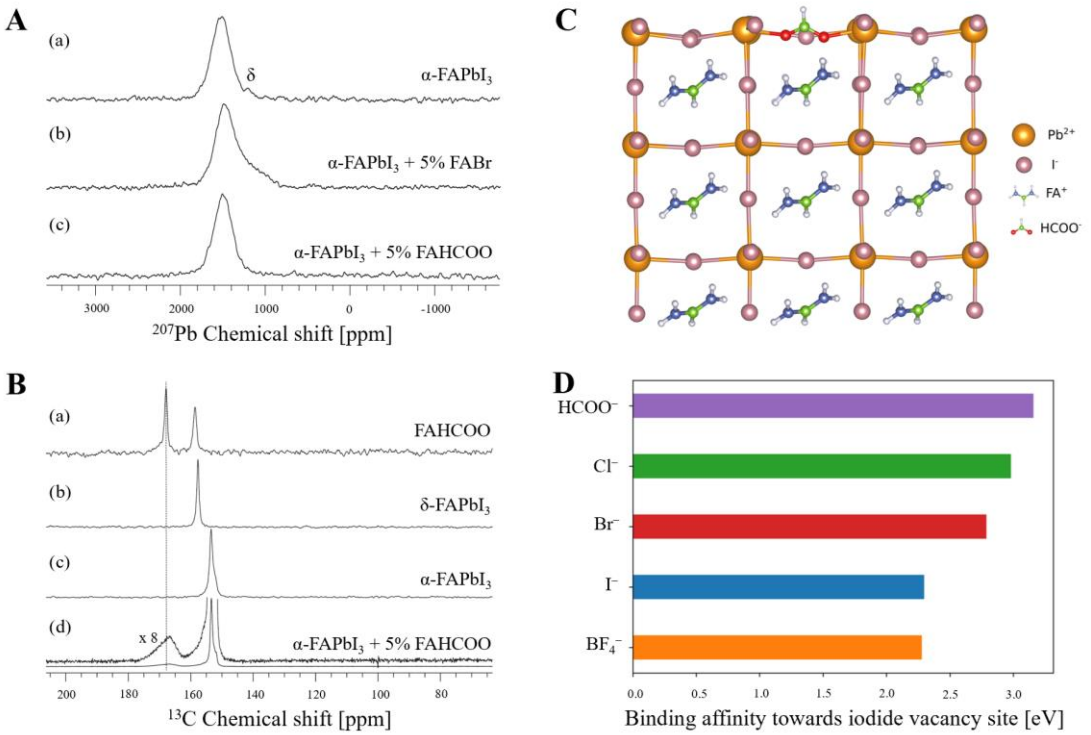

Figure 2. Solid-state NMR and MD simulations. (**A**) ^{207}Pb ssNMR measurements at 15 kHz MAS and 298 K for (a) α-$FAPbI_3$, (b) α-$FAPbI_3$ + 5% FABr, (c) α-$FAPbI_3$ + 5% FAHCOO. In (a) a small amount of the δ phase can be seen, but this is distinct from the shoulder seen in (b), and in any case is not seen in (c). (**B**) ^{13}C ssNMR measurements at 12 kHz MAS and 100K for (a) FAHCOO, (b) δ-$FAPbI_3$, (c) α-$FAPbI_3$, (d) α-$FAPbI_3$ + 5% FAHCOO (the upper trace is an 8-fold magnification). (**C**) Calculated structure showing passivation of an I^- vacancy at the $FAPbI_3$ surface by a $HCOO^-$ anion. All chemical species are shown with the balls and sticks representation. Pb^{2+} ions are shown with large yellow coloured spheres, I^- ions with light pink, oxygen atoms with red, carbon atoms with green, nitrogen atoms with blue and hydrogen atoms with white. (**D**) The binding affinities of different anions to the I^- vacancy at the surface.

To explore the local environment of the $HCOO^-$ anions in the Fo-$FAPbI_3$ perovskite, $^1H \rightarrow {}^{13}C$ cross-polarization (CP) experiments were performed at 100 K (*29*). Figure 2B(a) shows ^{13}C resonance signals at 167.8 ppm and 158.5 ppm for the $HCOO^-$ and FA^+ environments in FAHCOO. Figure 2B, (b) and (c) show the δ-$FAPbI_3$ and α-$FAPbI_3$ and ^{13}C resonances at 157.6 ppm and 153.4 ppm, respectively. Upon mixing 5 mol% FAHCOO with $FAPbI_3$, the ^{13}C signal of α-$FAPbI_3$ remained unchanged, at 153.4 ppm, shown in Fig. 2B(d), which further corroborates the lack of substitution of iodide by $HCOO^-$ inside the $FAPbI_3$ lattice. The $HCOO^-$ peak, however, exhibited significant broadening, indicative of a distribution of local environments which we attribute to the interaction of the $HCOO^-$ anion with undercoordinated Pb^{2+} via insertion in iodide vacancies present at the surface or grain boundaries of the perovskite, in contrast to the well-defined environment in crystalline FAHCOO. For the spin-coated 2% Fo-$FAPbI_3$ thin films, the formate ^{13}C signal is less intense, appearing as a shoulder on the peak of α-$FAPbI_3$ (fig. S6). This is due to a combination of the lower initial formate concentration and potentially greater evaporation of formate during annealing in the thin films compared to powders since the exposed area is greater, although the CP spectra are not quantitative. The presence of FAHCOO in the α-$FAPbI_3$ films is also supported by the time-of-flight secondary ion mass spectrometry (TOF-SIMS) measurements shown in fig. S7. We further quantified the composition of the spin-coated 2% Fo-$FAPbI_3$ films using directly-

detected ^{13}C NMR at 100 K (fig. S8). Integration of the FA^+ and MA^+ resonances in the quantitative ^{13}C spectrum yields 5.1% of the MA^+ ion in the final perovskite films (see Note 3 in the SM).

To explore in more detail the unique role of $HCOO^-$ anions, we performed *ab-initio* molecular dynamics (MD) simulations of a homogeneous mixture of different ions in the precursor solution (see Note 4 and fig. S9), comprising Pb^{2+}, I^-, $HCOO^-$, and FA^+, and found that the $HCOO^-$ anions coordinate strongly with the Pb^{2+} cations (Supplementary movie 1). This strong coordination might help in slowing down the growth process, resulting in larger stacked grains of the perovskite film, which is validated by the *in-situ* images of the perovskite films without annealing (fig. S10). Compared to the reference film, 2% Fo-$FAPbI_3$ film had a slower color change from brown to black. We also performed MD simulations to understand the surface passivation effects of $HCOO^-$ anions. Figure S11 shows a super cell of a α-$FAPbI_3$ perovskite slab with surface iodides replaced by formate anions. We found that $HCOO^-$ anions can form a nexus of hydrogen bonding with FA^+ ions (shown in fig. S11C and supplementary movie 2), in agreement with the hydrogen bonding in the FAHCOO crystal structures (*30*). In addition, $HCOO^-$ anions can also form a bonding network on the Pb^{2+} ion terminated surface because of their strong affinity towards lead (shown in fig. S11B and supplementary movie 3). Figure 2C shows a $HCOO^-$ anion passivating an I^- vacancy at the $FAPbI_3$ surface. We then calculated the binding affinity of the $HCOO^-$ anions to the I^- vacancies at the surface (figs. S12, S13 and S14 in the SM). I^- vacancy defects are the most deleterious defects for the stability of halide perovskites. The energies in Fig. 2D show that the $HCOO^-$ has the highest binding energy to I^- vacant sites at the interface compared to other anions including Cl^-, Br^-, I^- and BF_4^-. Furthermore, we have also calculated the bonding energies of formamidinium at the interface with formate anions and with other anions (see Note 5 in the SM and figs. S15 and S16). We found that FA^+ cations at the interface form a stronger bonding with $HCOO^-$ than with the other anions. One can conclude that the $HCOO^-$ anion acts as a passivating agent against the formation of vacancy defects (such as I^- and FA^+).

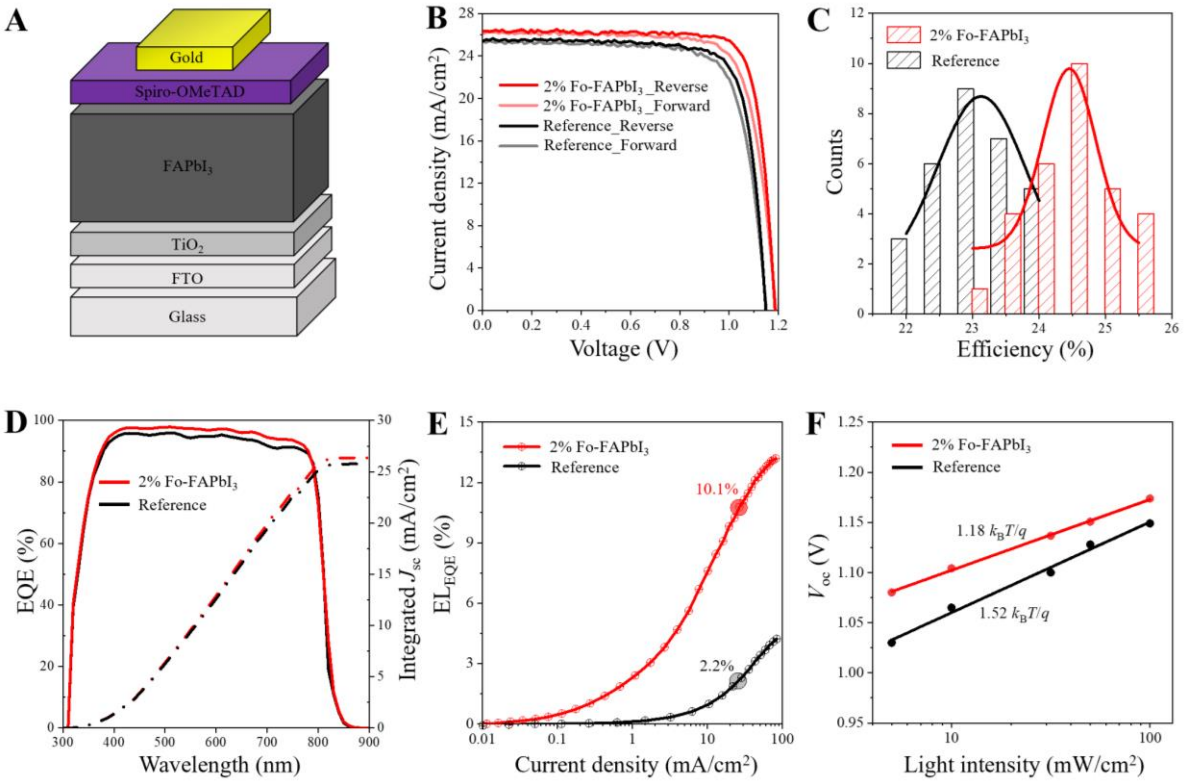

Figure 3. PV performance characterisation of the $FAPbI_3$ PSCs. (**A**) The configuration of a typical $FAPbI_3$ PSC device. (**B**) *J-V* curves of the reference and target PSCs under both reverse and forward scans. (**C**) The statistical distribution of the PCE of the reference and target PSCs. (**D**) EQE and the integrated J_{sc} of the reference and target PSCs. (**E**) EQE_{EL} measurements of the reference and target PSCs under a current density from 0.01 to 100 mA/cm^2. (**F**) The relationship between the measured V_{oc} and light intensity for the reference and target PSCs.

We further explored the photovoltaic (PV) performance of the reference and Fo-$FAPbI_3$ based PSCs. $FAPbI_3$ PSCs were fabricated using a FTO/TiO_2/$FAPbI_3$/Spiro-MeOTAD/Au (FTO, fluorine doped tin oxide; c-TiO_2; Spiro-MeOTAD, 2,2´,7,7´-tetrakis[*N*,*N*-bis(*p*-methoxyphenyl)amino]-9,9´-spirobifluorene) configuration as illustrated in Fig. 3A. Figure 3B shows *J-V* curves of the reference and target PSCs under both forward and reverse scans. The reference cell had a maximum PCE of 23.92% with a J_{sc} of 25.72 mA/cm^2, V_{oc} of 1.153 V and FF of 80.69%. The target PSC had a maximum PCE of 25.59% with a J_{sc} of 26.35 mA/cm^2, V_{oc} of 1.189 V and fill factor (FF) of 81.7%. The detailed parameters are summarized in Table 1 in the SM. The statistical distribution of the measured PCE of the reference and target PSCs are shown in Fig. 3C. It shows an average PCE of 23.2% and 24.4% for the reference and target PSCs, respectively. To verify the efficiency, we sent one of our best target PSCs to an accredited PV test laboratory (Newport, USA) for certification. Figures S17 and S18 represent a certified quasi-steady-state efficiency of 25.21% with a V_{oc} of 1.174 V, J_{sc} of 26.25 mA/cm^2 and FF of 81.8%.

EQE measurements (Fig. 3D) of the $FAPbI_3$ PSCs were performed to verify the measured J_{sc} above. The EQE of the target PSC was higher than that of the reference cell during the whole visible light absorption region. By integrating the EQE over the AM 1.5G standard spectrum, the projected J_{sc} of the reference and target PSCs are 25.75 and 26.35 mA/cm^2 respectively, which matches well with the measured J_{sc} under the solar simulator. Figure 3E shows the EQE of the electroluminescence (EQE_{EL}) of the reference and target PSCs. We know that a solar cell's photovoltage is directly related to the ability to extract its internal luminescence (*31*). EQE_{EL} has been successfully used to predict the V_{oc} of PSCs (*32*). The reference cell had an EQE_{EL} of 2.2%, while the target cell had an EQE_{EL} of 10.1% for an injection current density of 25.5 and 26.5 mA/cm^2 (corresponding to the J_{sc} measured under 1 sun illumination), respectively. Hence, the formate treatment reduces the non-radiative recombination rate 5 times. We derived a bandgap of 1.53 eV for the target film using the Tauc plot (fig. S19). The obtained V_{oc} of 1.21 V (shown in fig. S20) of the target cell shows a record 96.8% of the Shockley-Queisser limit V_{oc} (1.25 V) for an absorption threshold of 1.53 eV (*32*,*33*). To further confirm the role of formate, we also provided the PV performance of the devices fabricated using formamidinium acetate additive (fig. S21), which unfortunately showed a negative effect. For the devices fabricated without using MACl additives or passivation layers, formate containing devices still showed an advantage (fig. S22).

Figure S23, A and B present the *J-V* responses of the reference and target PSCs under different light intensities. Figure S23C shows a linear relationship (a slope of ~0.95) between J_{sc} and light intensity for both the reference and target PCSs, indicating good charge transport and negligible bimolecular recombination. Figure 3F shows the linear relationship between V_{oc} and the logarithm of light intensities of the $FAPbI_3$ PSCs. We fitted the data points with a slope of $n_{id}k_BT/q$, where n_{id} is the ideality factor, k_B is the Boltzmann constant, T is temperature, and q is the electric charge. The reference cell had an n_{id} of 1.52, while the target cell had an n_{id} of 1.18, which is lower than the previously reported 1.27 by Jiang. *et al* (*33*). A summary of the

detailed PV parameters is given in Table S2 in the SM. The reduced n_{id} indicates a reduced trap-assisted recombination (*34*, *35*), which is further supported by the space-charge limited current (SCLC) measurements (fig. S24). We know that for a solar cell where the shunt and series resistance are negligible, the FF depends only on the V_{oc} divided by $n_{id}k_BT/q$ (*36*). The reduced n_{id} in our case also contributes to the increased measured FF of the target PSCs.

To assess the stability of our PSCs, we measured first their shelf life by storing unencapsulated devices in the dark at 25 ℃ and 20% relative humidity. Figure 4A shows that the PCE of the reference cell decreased by about 35%, while there was only a 10% degradation for the 2% Fo-$FAPbI_3$ cell after 1000-hour aging. A heat stability test was also performed by annealing the unencapsulated PSC devices at 60 ℃ under 20% relative humidity. Figure 4B shows that the 2% Fo-$FAPbI_3$ solar cell retained about 80% of the initial efficiency after 1000-hour aging, while the reference cell retained only about 40%.

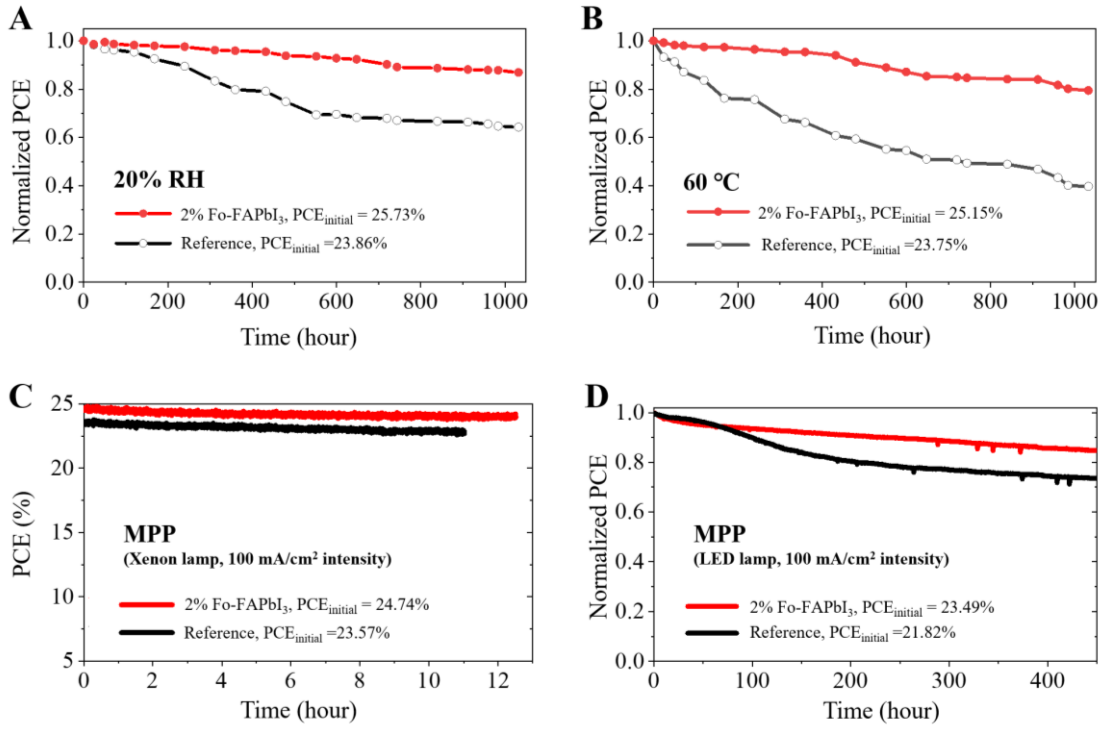

Figure 4. Stability test of the $FAPbI_3$ PSCs. (**A**) The shelf stability of the reference and 2% Fo-$FAPbI_3$ PSCs. (**B**) The heat stability of the reference and 2% Fo-$FAPbI_3$ PSCs. (**C**) The operational stability of the reference and one top performance 2% Fo-$FAPbI_3$ PSCs. (**D**) The long-term operational stability of the reference and 2% Fo-$FAPbI_3$ PSCs.

We further investigated the operational stability of the PSCs by aging the unencapsulated devices under nitrogen atmosphere at maximum power point (MPP) tracking condition under simulated one sun illumination. Figure 4C shows the PCE of the PSCs (top performance) under continuous light soaking using a Xenon lamp. The PCE of the 2% Fo-$FAPbI_3$ solar cell remained over 24% after 10-hour MPP tracking, while the PCE of the reference solar cell decreased down to 22.8%. Figure 4D shows the long-term operational stability of the PSCs. The PCE of the reference cell decreased by about 30%, while the 2% Fo-$FAPbI_3$ solar cell only lost about 15% of its initial efficiency. Note that in this study the temperature of the PSCs was measured to be around 35℃, as we did not cool the cells during illumination. We recorded the PV metrics of the devices every 30 mins. Compared to the 2% Fo-$FAPbI_3$ PSC, the reference cell had a significant decrease for J_{sc} and FF over the 450-hour MPP tracking test (fig. S25), suggesting less stable reference perovskite layer. The decline of FF resembles our previous

observation (*9*), where we attributed the decline in FF to a de-doping of the hole conductor due to Li ion migration from the Spiro-MeOTAD to the perovskite layer under illumination (*37*).

The relatively better thermal and operational stability of the target cell should be assigned to the improved crystallinity and reduced halide defects of the 2% Fo-$FAPbI_3$ perovskite films. We know that crystallinity is crucial for the stability of the perovskites as the main degradation process starts from defects near the grain boundaries. The high crystallinity and large grain size of the formate containing perovskite films (validated by the SEM and XRD measurements) suggest fewer grain boundaries, which will contribute to greater stability and performance. Importantly, our simulations and calculations suggest that formate anions have the highest binding affinity to iodide vacancy sites among all halides/pseudo halides thus are the best candidates to eliminate the most abundant and deleterious lattice defects present in halide perovskite films resulting in a dramatic reduction of the trap concentration (validated by SCLC, TRPL and EQE_{EL} measurements). The low level of halide vacancies benefits the stability of the solar cells, as halide vacancies could also act as a main degradation pathway due to photo-induced iodine loss, especially under light illumination.

References

(1) Kojima, A. et al. Organometal halide perovskites as visible-light sensitizer for photovoltaic cells. *J. Am. Chem. Soc*. **131**, 6050-6051 (2009).
(2) Grätzel, M. et al. The light and shade of perovskite solar cells. *Nature Materials* **13**, 838-842 (2014).
(3) Park, N.-G. et al. Towards stable and commercially available perovskite solar cells. *Nature Energy* **1**, 16152 (2016).
(4) Correa-Baen, J.-P. et al. Promises and challenges of perovskite solar cells. *Science* **358**, 739-744 (2017).
(5) Lu, H. et al. Compositional and interface engineering of organic-inorganic lead halide perovskite solar cells. *iScience* **23**, 101359 (2020).
(6) Eperon, G. E. et al. Formamidinium lead trihalide: a broadly tunable perovskite for efficient planar heterojunction solar cells. *Energy Environ. Sci.* **7**, 982-988 (2014).
(7) Pellet, N. et al. Mixed-organic-cation perovskite photovoltaics for enhanced solar-light harvesting. *Angew. Chem. Int. Ed.* **53**, 3151-3157 (2014).
(8) Jeon, N. J. et al. Compositional engineering of perovskite materials for high-performance solar cells. *Nature* **517**, 476-480 (2015).
(9) Lu, H. et al. Vapor-assisted deposition of highly-efficient, stable black phase $FAPbI_3$ perovskite solar cells. *Science* **370**, eabb8985 (2020).
(10) De Wolf, S. et al. Organometal halide perovskites: sharp optical absorption edge and its relation to photovoltaic performance. *J. Phys. Chem. Lett.* **5**, 1035-1039 (2014).
(11) Stranks, S. D. et al. Electron-hole diffusion lengths exceeding 1 micrometer in an organometal trihalide perovskite absorber. *Science* **342**, 341-344 (2013).
(12) M. Herz, L. et al. Charge-carrier mobilities in metal halide perovskites: fundamental mechanisms and limits. *ACS Energy Lett*. **2**, 1539-1548 (2017).
(13) www.nrel.gov/pv/cell-efficiency.html.
(14) Zheng, X. et al. Managing grains and interfaces via ligand anchoring enables 22.3%-efficiency inverted perovskite solar cells. *Nature Energy* **5**, 131-140 (2020).
(15) Liu, Z. et al. A holistic approach to interface stabilization for efficient perovskite solar modules with over 2000-hour operational stability. *Nature Energy* **5**, 596-604 (2020).
(16) Saliba, M. et al. Cesium-containing triple cation perovskite solar cells: improved stability, reproducibility and high efficiency. *Energy. Environ. Sci.* **9**, 1989-1997 (2016).

(17) Kim, M. et al. Methylammonium chloride induces intermediate phase stabilization for efficient perovskite solar cells. *Joule* **3**, 1-14 (2019).
(18) Min, H. et al. Efficient, stable solar cells by using inherent bandgap of α-phase formamidinium lead iodide. *Science* **366**, 749-753 (2019).
(19) Yang, S. et al. Thiocyanate assisted performance enhancement of formamidinium based planar perovskite solar cells through a single one-step solution process. *J. Mater. Chem. A* **4**, 9430-9436 (2016).
(20) Kim, D. H. et al. Bimolecular additives improve wide-band-gap perovskites for efficient tandem solar cells with CIGS. *Joule* **3**, 1734-1745 (2019).
(21) Kim, D. et al. Efficient, stable silicon tandem cells enabled by anion-engineered wide-bandgap perovskites. *Science* eaba3433 (2020).
(22) Walker, B. et al. Pseudohalides in lead-based perovskite semiconductors. *Adv. Mater.* **31**, 1807029 (2019).
(23) T. Moore, D. et al. Direct crystallization route to methylammonium lead iodide perovskite from an ionic liquid. *Chem. Mater*. **27**, 3197-3199 (2015).
(24) Seo, J. et al. Ionic liquid control crystal growth to enhance planar perovskite solar cells efficiency. *Adv. Energy Mater*. **6**, 1600767 (2016).
(25) K. Nayak, P. et al. Mechanism for rapid growth of organic-inorganic halide perovskite crystals. *Nat Commun*. **7**, 13303 (2016).
(26) Meng, L. et al. Improved perovskite solar cell efficiency by tuning the colloidal size and free ion concentration in precursor solution using formic acid additive. *Journal of Energy Chemistry*. **41**, 43-51 (2020).
(27) Khan, Y. et al. Waterproof perovskites: high fluorescence quantum yield and stability from a methylammonium lead bromide/formate mixture in water. *J. Mater. Chem. C* **8**, 5873-5881 (2020).
(28) Askar, A. et al. Composition-tunable formamidinium lead mixed halide perovskites via solvent-free mechanochemical synthesis: decoding the Pb environments using solid-state NMR spectroscopy. *J. Phys. Chem. Lett*. **9**, 2671-2677 (2018).
(29) J. Kubicki, D. et al. Cation Dynamics in Mixed-Cation $(MA)_x(FA)_{1-x}PbI_3$ Hybrid Perovskites from Solid-State NMR. *J. Am. Chem. Soc*. **139**, 10055-10061 (2017).
(30) Zhou, Z. et al. Synthesis, microwave spectra, x-ray structure, and high-level theoretical calculations for formamidinium formate. *J. Chem. Phys*. **150**, 094305 (2019).
(31) Ross, R. et al. Some Thermodynamics of Photochemical Systems. *J. Chem. Phys.* **46**, 4590-4593 (1967).
(32) Tress, W. et al. Predicting the open-circuit voltage of $CH_3NH_3PbI_3$ perovskite solar cells using electroluminescence and photovoltaic quantum efficiency spectra: the role of radiative and non-radiative recombination. *Adv. Energy Mater*. **5**, 1400812 (2015).
(33) Jiang, Q. et al. Surface passivation of perovskite film for efficient solar cells. *Nat. Photonic* **13**, 460-466 (2019).
(34) Yang, D. et al. Surface optimization to eliminate hysteresis for record efficiency planar perovskite solar cells. *Energy Environ. Sci*. **9**, 3071-3078 (2016).
(35) Kuik, M. et al. Trap-assisted recombination in disordered organic semiconductors. *Phys. Rev. Lett.* **107**, 256805 (2011).
(36) Green, M. Accuracy of analytical expressions for solar cell fill factors. *Solar cells*. **7**, 337-340 (1982).
(37) Wang, Y. et al. Stabilizing heterostructures of soft perovskite semiconductors. *Science* **365**, 687-691 (2019).

Data availability: The data that support the findings of this study are available from the corresponding author upon reasonable request.

Code availability: The code used for this study are available from the corresponding author upon reasonable request.

Acknowledgements: We thank beamline BL17B1, BL14B1, BL11B, BL08U and BL01B1 staff at the SSRF for providing the beamline. This research was supported by the Technology Development Program to Solve Climate Changes of the National Research Foundation (NRF) funded by the Ministry of Science, ICT & Future Planning (2020M1A2A2080746), "the Research Project Funded by U-K Brand" (1.200030.01) of Ulsan National Institute of Science & Technology (UNIST) and the Development Program of the Korea Institute of Energy Research (KIER) (C0-2401 and C0-2402). J.J. and H.L. acknowledge the financial support from the GRAPHENE Flagship Core 2 project supported by the European Commission H2020 Program under contract 785219. L.E. acknowledges support from the Swiss National Science Foundation. U.R. acknowledges funding from the Swiss National Science Foundation via individual grant No. 200020_185092 and the NCCR MUST. A.H. acknowledges the Swiss National Science Foundation, project "Fundamental studies of dye-sensitized and perovskite solar cells" with project No 200020_185041. M.G. acknowledges financial support from the European Union's Horizon 2020 research and innovation programme under grant agreement No 881603 and the King Abdulaziz City for Science and Technology (KACST).

Author contributions: We thank W.R.Tress for useful discussions. J.J., B.W. and J.Y.K. had the idea of this project. J.J., M.K. and H.L. prepared the samples, did the relevant PV measurements, analysed the data, and wrote the manuscript. J.S. synthesised the FAHCOO material. M.K. and D.S.K. certified the efficiency of the PSCs. Y.J.Y. measured PL and UV-vis spectroscopy. S.J.C. and I.W.C. did the TRPL, SEM and XRD measurements. Y.J. and H.L. collected the light intensity dependent *J-V* data. M.K. and J.H.L contributed to the DFT calculations. P.A. and U.R. were responsible for the MD simulations. A.M., M.A.H. and L.E. conducted the ssNMR measurements and analysis. B.P.D. performed the AFM measurements. H.L. conducted the long-term operational stability measurements, EQE_{EL} measurements and analysed the data. Y.Y. performed the 2D-GIXRD measurements. F.T.E contributed to the analysis of the TRPL data. S.M.Z. coordinated the project. A.H. and M.G. proposed experiments and wrote the final version. A.H., D.S.K., M.G. and J.Y.K. directed the work. All authors analysed the data and contributed to the discussions.